Zeng et al. Visual Computing for Industry, Biomedicine, and Art (2020) 3:10
https://doi.org/10.1186/s42492-020-00048-8

Visual Computing for Industry, Biomedicine, and Art

ORIGINAL ARTICLE Open Access

Poisson-noise weighted filter for time-of-flight positron emission tomography

Gengsheng L. Zeng[1,2*], Li Lv[3] and Qiu Huang[3]

Abstract

Image reconstruction for list-mode time-of-flight (TOF) positron emission tomography (PET) can be achieved by analytic algorithms. The backprojection filtering (BPF) algorithm is an efficient algorithm for this task. The conventional noise control method for analytic image reconstruction is the use of a stationary lowpass filter, which does not model the Poisson noise properly. This study proposes a nonstationary filter for Poisson noise control. The filter is implemented in the spatial domain in a form similar to convolution.

Keywords: Positron emission tomography, Time-of-flight, Analytic reconstruction, Noise control, Nonstationary filter

Introduction

Analytic image reconstruction methods for list-mode time-of-flight (TOF) positron emission tomography (PET) have been developed over the years [1–4]. One of the advantages of using TOF technology is its ability to reduce the image noise. If an iterative algorithm is used to reconstruct the image, the Poisson noise model is readily implemented as a weighting function for the projections [2]. For analytic reconstruction, the conventional noise control method is the application of a lowpass filter [5]. A lowpass filter is normally shift-invariant and can be implemented as convolution in the spatial domain or as multiplication in the Fourier domain [6]. The conventional lowpass filters thus are unable to model the Poisson noise accurately, because Poisson noise in an image is not stationary.

The goal of this study is to develop a nonstationary (i.e., shift variant) filter for Poisson noise control in analytic TOF PET image reconstruction. The filter can be two-dimensional (2D) or three-dimensional (3D). The filter developed in this study is specially targeted towards the backprojection filtering (BPF) algorithm used for TOF PET reconstruction [3, 4]. In the BPF algorithm, each event is first backprojected into the image domain. This backprojection can add a value only to one point in the image domain or add a one-dimensional (1D) Gaussian function along the line-of-response (LOR), where the point or the peak of the 1D Gaussian is at the location determined by the TOF information.

It is understood that the TOF information is not accurate and has some uncertainty. This uncertainty can be modeled as a 1D Gaussian function with a standard deviation of σ_1. The TOF backprojection puts a different 1D Gaussian function along the LOR, and this backprojection Gaussian function can be characterized by its standard deviation σ_2. As pointed out in refs. [3, 4], σ_2 and σ_1 are independent, and the user has freedom to choose σ_2. The combined effect of σ_1 and σ_2 will be inverted by the tomographic filter, which depends on the sum of $\sigma_1 + \sigma_2$. Using today's typical TOF uncertainty value, the tomographic filter can be approximated by a ramp filter (also known as the ρ filter).

Let $\sigma_2 = 0$, which means that the TOF backprojector adds each event to a point in the image domain. The location of the point may not be the true location where the positron/electron annihilation happens due to the TOF information uncertainty. Clearly, the TOF backprojected image contains the accumulation of the photon counts at each pixel, and the noise follows the Poisson distribution. This is also true for $\sigma_2 > 0$. The mean value

* Correspondence: larry.zeng@uvu.edu; larryzeng@live.com
[1]Department of Engineering, Utah Valley University, 800 West University Parkway, Orem, UT 84058, USA
[2]Department of Radiology and Imaging Sciences, University of Utah, 729 Arapeen Drive, Salt Lake City, UT 84108, USA
Full list of author information is available at the end of the article

Springer Open

© The Author(s). 2020 **Open Access** This article is licensed under a Creative Commons Attribution 4.0 International License, which permits use, sharing, adaptation, distribution and reproduction in any medium or format, as long as you give appropriate credit to the original author(s) and the source, provide a link to the Creative Commons licence, and indicate if changes were made. The images or other third party material in this article are included in the article's Creative Commons licence, unless indicated otherwise in a credit line to the material. If material is not included in the article's Creative Commons licence and your intended use is not permitted by statutory regulation or exceeds the permitted use, you will need to obtain permission directly from the copyright holder. To view a copy of this licence, visit http://creativecommons.org/licenses/by/4.0/.

and the variance are the same for a Poisson distributed random variable.

Methods Section develops a nonstationary filter for the Poisson noise. Some 2D computer simulations are presented in Results Section. The following is Discussion Section, and Conclusions Section concludes the study. The Matlab® code for the proposed filter is presented in the Appendix.

Methods

This section develops a nonstationary filter for the 2D case. The 3D case is similar and can be readily obtained without any difficulties. Let f be the unfiltered image and h be the filter kernel. The conventional linear shift-invariant filter can be expressed as a convolution integral

$$g(x,y) = \iint h(x-u, y-v) f(u,v)\, dudv \tag{1}$$

where $g(x, y)$ is the filtered image. In Eq. (1), the kernel h is shift-invariant. In other words, the shift-invariant filter blurs the image f with the same kernel h everywhere. If the kernel h varies from location to location, Eq. (1) can be modified to

$$g(x,y) = \iint h(u,v;x,y) f(u,v)\, dudv \tag{2}$$

Equation (2) is no longer a convolution. The calculation complexity of Eq. (2) is almost the same as the complexity of Eq. (1), except that in Eq. (2) the kernel h must be evaluated differently for different locations (x, y).

In this study, we assume the filter kernel h to be a 2D Gaussian function with a standard deviation $\sigma(x, y)$. This 2D Gaussian filter with $\sigma(x, y)$ is different form the 1D TOF uncertainty Gaussian function with σ_1 and is also different from the 1D TOF backprojection Gaussian function with σ_2.

Let us further assume that f is a TOF backprojected image using $\sigma_2 = 0$. The image f contains Poisson noise. Each pixel of f is treated as a Poisson distributed random variable, and hence the variance of a pixel in f is the mean value of the pixel. In practice, the mean value of each pixel of f is unknown, because we only have one noise realization. We thus assume that the mean value is the one realization of the image intensity of f.

Our strategy is to use a large kernel size of h if the corresponding f value is large and a small kernel size if the corresponding f value is small. The kernel size $\sigma(x, y)$ is thus a monotonic function of the image pixel $f(x, y)$. In this study, we empirically propose

$$\sigma(x,y) = a \times f(x,y)^b + c \tag{3}$$

where $\sigma(x, y)$ is the standard deviation value for the multidimensional Gaussian kernel h at pixel (x, y). In Eq. (3), a, b and c are user-selected parameters.

As a special case of $a = 0$, h has a constant $\sigma(x, y)$, the filter is shift invariant, and Eq. (2) reduces to Eq. (1).

Results

Computer simulations were carried out using the Shepp-Logan phantom [7]. The image size was 256×256. This Shepp-Logan image was assumed to be the TOF back-projected image. Poisson noise was incorporated into the image. The original noisy image was shown in Fig. 1. Two filtered images are shown in Figs. 2 and 3, respectively. In Fig. 2, a shift-invariant filter was used with $a = 0$ and $c = 0.73$, where $c = 0.73$ was the optimal value in terms of the root-mean-square-error (RMSE) when a was set to 0. In Fig. 3, a nonstationary filter was used with $a = 0.175$, $b = 0.01$, and $c = 0.6$.

The RMSE was calculated for each of these 3 images compared to the true image. The RMSE's for Figs. 1, 2 and 3 are 1.0759, 0.6093, and 0.6010, respectively. The RMSE has been reduced by switching the stationary filter to the nonstationary filter.

Discussion

A unique feature of the proposed denoising algorithm is its non-stationarity. The non-stationary noise exists in PET and in other imaging modalities. Similar to PET, the noise in single photon emission computed tomography (CT) also contains Poisson noise [8]. In x-ray CT, the line-integral data is the logarithm of the Poisson noise corrupted transmission measurements, and the noise variance is spatially varying. Its noise variance can be approximated by an exponential function of the measurements [8]. Speckling noise in medical ultrasound

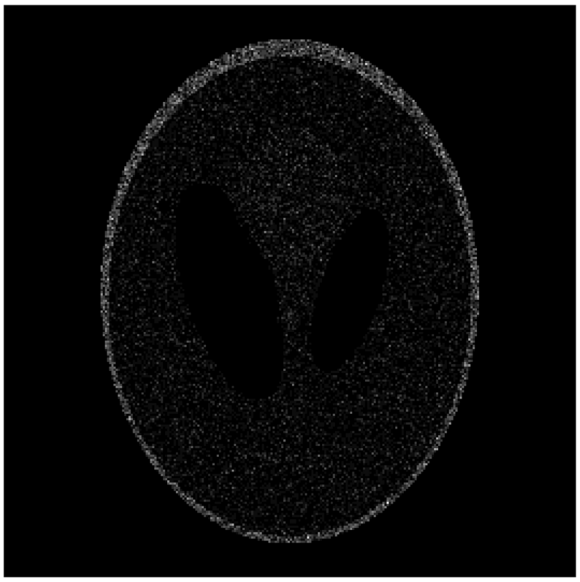

Fig. 1 The original noisy image, where the Shepp-Logan phantom is corrupted by the Poisson noise. The RMSE is 1.0759

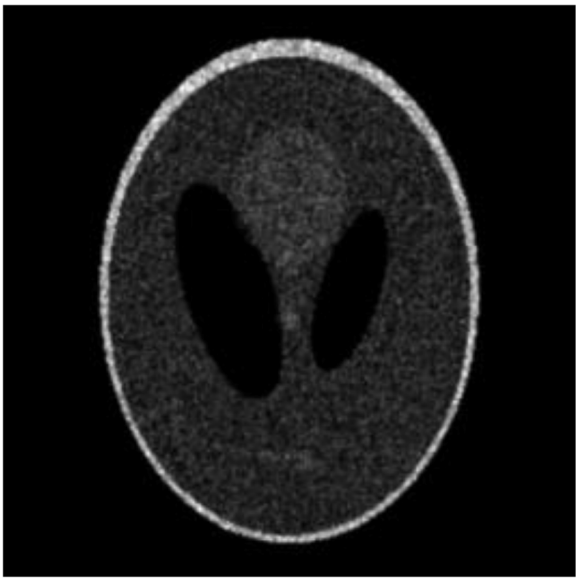

Fig. 2 The filtered image, where a shift-invariant filter is applied with $a = 0$ and $c = 0.73$ in Eq. (3). The RMSE is 0.6093

images is nonstationary with a multiplicative noise model [9]. The denoising algorithm developed in this study can be readily modified to these applications. Of course, if the image noise is additive and stationary, there is no need to use the proposed algorithm. A common bandpass filter or lowpass filter may be sufficient for the denoising purpose. The stationary filters are much faster than the algorithm developed in this study. An example of such an imaging modality is photoacoustic imaging [10–12], which has an additive noise model and the noise variance is approximately stationary. Other advantages of photoacoustic imaging are that it does not use ionizing radiations and it has very high spatial resolution.

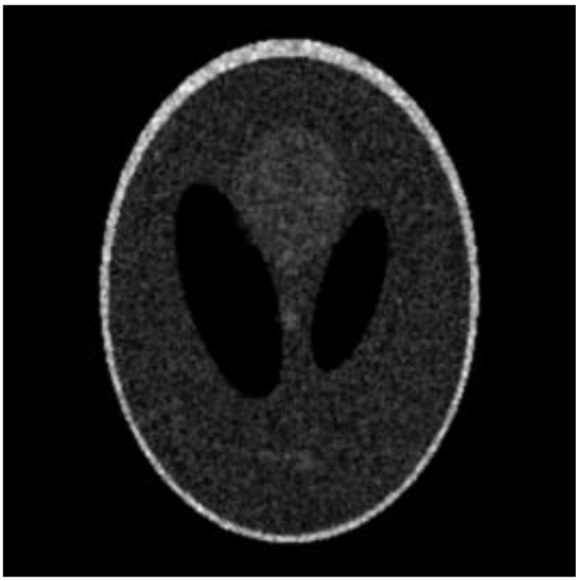

Fig. 3 The filtered image, where a nonstationary filter is applied with $a = 0.175$, $b = 0.01$ and $c = 0.6$ in Eq. (3). The RMSE is 0.6010

Nowadays deep learning is the most active research area, and much work has been reported in PET denoising [13–19]. Deep learning denoising is effective and has better results than traditional methods. One popular approach is the post-processing neural network that improves the signal-to-noise ratio in the raw reconstruction, which is obtained by using the filtered backprojection algorithm or the ordered-subset expectation-maximization algorithm. As a result, the low-dose PET images may have the image quality of the regular-dose PET. Instead of post-processing, another approach is to use the neural network for image reconstruction. Deep learning methods require data pairs to train the network. Good results are based on whether the current data is closely relevant to the training data sets. Our proposed algorithm is not a machine learning approach and does not require any data to train. The requirement of using our developed algorithm is that we need to know how the image noise variance dependency on the mean image. This means image is replaced by the raw image in practice. For the BPF PET image reconstruction, the raw image is the backprojected image (before the tomographic filter is applied).

Conclusions

This study develops a nonstationary filter for the list-mode TOF PET's BPF image reconstruction algorithm. The BPF algorithm consists of two steps: TOF backprojection and tomographic filtering. The proposed denoising filter is applied between these two steps. In other words, the nonstationary filter is applied to the TOF backprojected image.

The filter can be 2D or 3D, and its kernel width depends linearly on the intensity of the TOF backprojected image according to Eq. (3). The user needs to select parameters a and b according to the noise level and experiences. When $a = 0$, the filter degenerates to a shift-invariant filter.

Appendix

Matlab Code for the proposed nonstationary filter

```
% Larry, 12/17/2019% TOF PET Post Filter.
  hsize = 11; % kernel size (odd int).
  h2 = floor (hsize/2); % half kernel size.
  isize0 = 256; % image size.
  % Try (1) a = 0, c = 0.73 (RMSE = 0.6093); (2) a = 0.175,
b = 0.01, c = 0.6% (RMSE = 0.6010); Original noisy image
RMSE = 1.0759.
  a = 0.;
  b = 0.01;
  c = 0.73;
```

```
rng (1); % random number seeding.
ph 0 = 10 * phantom (isize0); % Sepp-Logan phantom.
ph = padarray (ph 0, [h2 h2]); % Pad zeros.
ph = imnoise (ph*1e-12,' poisson') * 1e12; % Add Poisson noise.
im_out = zeros (size (ph)); % Output initialization.
Figure (2), imshow (ph, []), title ('noisy image').
for i = h2 + 1:isize0 + h2.
for j = h2 + 1:isize0 + h2.
temp = ph (i-h2:i + h2, j-h2:j + h2); % image patch.
sigma = a * (ph (i, j)).^b + c; % kernel width.
h = fspecial ('gaussian', hsize, sigma); % Filter kernel.
im_out (i, j) = dot (h(:), temp (:)); % inner product.
end
end
Figure (4), imshow (im_out, []), title ('filtered image').
I = im_out;
imax = max (I (:));
imin = min(I (:));
I = (I - imin)/(imax - imin);
% imwrite (I,' a175b01c61.tif') % RMSE 0.6010.
imwrite (I,' a0c73.tif') % RMSE 0.6093.
I = ph;
imax = max (I (:));
imin = min (I (:));
I = (I - imin)/(imax - imin);
imwrite (I,' noisyImage.tif').
ph 1 = padarray (ph 0, [h2 h2]);
ph 1 = (ph 1-im_out).^2;
MSE = sqrt (sum(ph 1(:))/ length (ph 1(:))) % RMSE.
ph 1 = padarray (ph 0, [h2 h2]);
ph 1 = (ph-ph 1).^2;
noisyMSE = sqrt (sum (ph 1(:))/ length (ph 1(:))) % RMSE.
```

Abbreviations

CT: Computed tomography; PET: Positron emission tomography; TOF: Time-of-flight; LOR: Line-of-response; 1D: One-dimensional; 2D: Two-dimensional; 3D: Three-dimensional; BPF: Backprojection filtering; RMSE: Root-mean-square-error

Acknowledgements

Not applicable.

Authors' contributions

All authors read and approved the final manuscript.

Funding

Not applicable.

Availability of data and materials

Not applicable.

Competing interests

None of the authors have any competing interests in the manuscript.

Author details

[1]Department of Engineering, Utah Valley University, 800 West University Parkway, Orem, UT 84058, USA. [2]Department of Radiology and Imaging Sciences, University of Utah, 729 Arapeen Drive, Salt Lake City, UT 84108, USA. [3]School of Biomedical Engineering, Shanghai Jiaotong University, Shanghai 200240, China.

Received: 6 January 2020 Accepted: 14 April 2020
Published online: 29 April 2020

References

1. Tomitani T (1981) Image reconstruction and noise evaluation in photon time-of-flight assisted positron emission tomography. IEEE Trans Nucl Sci 28(6):4581–4589. https://doi.org/10.1109/TNS.1981.4335769
2. Conti M, Bendriem B, Casey M, Chen M, Kehren F, Michel C et al (2005) First experimental results of time-of-flight reconstruction on an LSO PET scanner. Phys Med Biol 50:4507–4526. https://doi.org/10.1088/0031-9155/50/19/006
3. Zeng GL, Li Y, Huang Q (2019) Analytic time-of-flight positron emission tomography reconstruction: two-dimensional case. Visual Comput Ind Biomed Art 2:22. https://doi.org/10.1186/s42492-019-0035-4
4. Zeng GL, Li Y, Huang Q (2020) Analytic time-of-flight positron emission tomography reconstruction: three-dimensional case. Visual Comput Ind Biomed Art 3:5. https://doi.org/10.1186/s42492-020-0042-5
5. Gonzalez RC, Woods RE (2018) Digital image processing, 4th edn. Pearson, New York
6. Zeng GL (2009) Medical image reconstruction: a conceptual tutorial. Springer, London
7. Shepp LA, Logan BF (1974) The Fourier reconstruction of a head section. IEEE Trans Nucl Sci 21(3):21–43. https://doi.org/10.1109/TNS.1974.6499235
8. Cherry SR, Sorenson JA, Phelps ME (2012) Physics in nuclear medicine, 4th edn. Elsevier Inc., Philadelphia. https://doi.org/10.1016/C2009-0-51635-2
9. Hsieh J (2003) Computed tomography: principles, design, artifacts, and recent advances. SPIE Press, Washington
10. Michailovich OV, Tannenbaum A (2006) Despeckling of medical ultrasound images. IEEE Trans Ultrason Ferroelectr Freq Control 53(1):64–78. https://doi.org/10.1109/TUFFC.2006.1588392
11. Nasiriavanaki M, Xia J, Wan HL, Bauer AQ, Culver JP, Wang LV (2014) High-resolution photoacoustic tomography of resting-state functional connectivity in the mouse brain. Proc Natl Acad Sci U S A 111(1):21–26. https://doi.org/10.1073/pnas.1311868111
12. Mozaffarzadeh M, Mahloojifar A, Orooji M, Adabi S, Nasiriavanaki M (2018) Double-stage delay multiply and sum beamforming algorithm: application to linear-array photoacoustic imaging. IEEE Trans Biomed Eng 65(1):31–42. https://doi.org/10.1109/TBME.2017.2690959
13. Gong K, Berg E, Cherry SR, Qi JY (2020) Machine learning in PET: from photon detection to quantitative image reconstruction. Proc IEEE 108(1):51–68. https://doi.org/10.1109/JPROC.2019.2936809
14. Kim K, Wu DF, Gong K, Dutta J, Kim JH, Son YD et al (2018) Penalized PET reconstruction using deep learning prior and local linear fitting. IEEE Trans Med Imaging 37(6):1478–1487. https://doi.org/10.1109/TMI.2018.2832613
15. Wang TH, Lei Y, Fu YB, Curran WJ, Liu T, Yang XF (2020) Machine learning in quantitative PET imaging. arXiv
16. Hashimoto F, Ohba H, Ote K, Teramoto A, Tsukada H (2019) Dynamic PET image denoising using deep convolutional neural networks without prior training datasets. IEEE Access 7:96594–96603. https://doi.org/10.1109/ACCESS.2019.2929230
17. Wang Y, Yu BT, Wang L, Zu C, Lalush DS, Lin WL et al (2018) 3D conditional generative adversarial networks for high-quality PET image estimation at low dose. NeuroImage 174:550–562. https://doi.org/10.1016/j.neuroimage.2018.03.045
18. Xiang L, Qiao Y, Nie D, An L, Lin WL, Wang Q et al (2017) Deep auto-context convolutional neural networks for standard-dose PET image estimation from low-dose PET/MRI. Neurocomputing 267:406–416. https://doi.org/10.1016/j.neucom.2017.06.048
19. Lu WZ, Onofrey JA, Lu YH, Shi LY, Ma TY, Liu YQ et al (2019) An investigation of quantitative accuracy for deep learning based denoising in oncological PET. Phys Med Biol 64(16):165019. https://doi.org/10.1088/1361-6560/ab3242

Publisher's Note

Springer Nature remains neutral with regard to jurisdictional claims in published maps and institutional affiliations.